

Drop impact on superheated surfaces: from capillary dominance to nonlinear advection dominance

Pierre Chantelot^{1,†} and Detlef Lohse^{1,2}

¹Physics of Fluids Group, Max Planck Center for Complex Fluid Dynamics, and J. M. Burgers Center for Fluid Dynamics, University of Twente, P.O. Box 217, 7500AE Enschede, Netherlands

²Max Planck Institute for Dynamics and Self-Organisation, Am Fassberg 17, 37077 Göttingen, Germany

(Received 24 November 2022; revised 6 March 2023; accepted 27 March 2023)

Ambient air cushions the impact of drops on solid substrates, an effect usually revealed by the entrainment of a bubble, trapped as the air squeezed under the drop drains and liquid–solid contact occurs. The presence of air becomes evident for impacts on very smooth surfaces, where the gas film can be sustained, allowing drops to bounce without wetting the substrate. In such a non-wetting situation, Mandre & Brenner (*J. Fluid Mech.*, vol. 690, 2012, p. 148) numerically and theoretically evidenced that two physical mechanisms can act to prevent contact: surface tension and nonlinear advection. However, the advection dominated regime has remained hidden in experiments as liquid–solid contact prevents rebounds being realised at sufficiently large impact velocities. By performing impacts on superheated surfaces, in the so-called dynamical Leidenfrost regime (Tran *et al.*, *Phys. Rev. Lett.*, vol. 108, issue 3, 2012, p. 036101), we enable drop rebound at higher impact velocities, allowing us to reveal this regime. Using high-speed total internal reflection, we measure the minimal gas film thickness under impacting drops, and provide evidence for the transition from the surface tension to the nonlinear inertia dominated regime. We rationalise our measurements through scaling relationships derived by coupling the liquid and gas dynamics, in the presence of evaporation.

Key words: drops, condensation/evaporation, multiphase flow

† Email address for correspondence: p.r.a.chantelot@utwente.nl

1. Introduction

Drop impacts are omnipresent in nature and industry (Yarin 2006; Josserand & Thoroddsen 2016; Lohse 2022). Yet, until the seminal experiments of Xu, Zhang & Nagel (2005) exposed the dramatic influence of ambient pressure on splashing, the influence of air on drop impact processes remained largely neglected. Indeed, predicting most macroscopic quantities associated with drop impact, such as the spreading dynamics (Riboux & Gordillo 2014; Gordillo, Riboux & Quintero 2019) or the maximal liquid imprint (Laan *et al.* 2014; Wildeman *et al.* 2016), does not require us to take into account the mediating role of air, i.e. of a surrounding medium. The interaction mechanism between the impacting drop and the solid substrate works as follows: as the drop approaches, pressure builds up in the air trapped between the liquid and the substrate, deforming the drop interface which adopts a dimple shape (Mandre, Mani & Brenner 2009; Hicks & Purvis 2010; Mani, Mandre & Brenner 2010; Bouwhuis *et al.* 2012; van der Veen *et al.* 2012). The edge of this central dimple region, the so-called neck, spreads radially as it moves downwards, and becomes increasingly sharp (Mandre *et al.* 2009; Mani *et al.* 2010; Duchemin & Josserand 2011; Kolinski *et al.* 2012). In most situations, air drains and liquid–solid contact occurs at the neck, resulting in the wetting of the substrate, and in the entrapment of a central bubble (Chandra & Avedisian 1991; Thoroddsen *et al.* 2005), which gives a subtle clue to the mediating role of air. Experiments and theory suggest that this scenario is the relevant one for splashing, where the influence of air manifests itself at later times, as the liquid is radially ejected along the substrate (Driscoll & Nagel 2011; Riboux & Gordillo 2014). In remarkable cases, such as low velocity impacts on smooth surfaces (Reynolds 1881; Pan & Law 2007; Kolinski, Mahadevan & Rubinstein 2014a) or in the dynamic Leidenfrost regime (Leidenfrost 1756; Tran *et al.* 2012; Quéré 2013), the intervening gas layer prevents contact and allows drop rebound, strikingly affecting the outcome of impacts.

Understanding the role played by the surrounding medium is crucial in applications such as inkjet printing or in immersion lithography, where air entrapment is undesirable (Switkes *et al.* 2005; Lohse 2022), or cooling processes, where heat transfer is strongly reduced in the presence of a gas layer (Kim 2007; Breitenbach, Roisman & Tropea 2018). In this article, we focus on non-wetting situations, and set out to exhibit the physical mechanisms that prevent the initial drainage of the gas trapped between the drop and the surface. Two effects have been theoretically and numerically shown to hinder the neck's downward motion: capillarity and nonlinear advection (Mandre & Brenner 2012). However, experiments on substrates kept at ambient temperature are limited to the regime where surface tension dominates the behaviour at the neck, as liquid–solid contact occurs when the impact velocity is increased (De Ruiter *et al.* 2012). Here, we perform impacts on superheated substrates, where vapour generation allows for contactless drop rebound for a large range of impact velocities and substrate temperatures (Tran *et al.* 2012; Shirota *et al.* 2016), with the goal of experimentally accessing the nonlinear advection dominated regime. We stress that our results are not relevant to determining the critical velocity for the occurrence of contact, which is driven by additional physics, such as rarefied gas effects and van der Waals interactions in idealised situations (Chubynsky *et al.* 2020), substrate roughness or contamination in experiments (Kolinski *et al.* 2014a) or instabilities of the vapour layer in the superheated case (Chantelot & Lohse 2021; Harvey, Harper & Burton 2021).

The paper is organised as follows. In § 2, we detail the experimental set-up and control parameters. We next discuss the phenomenology of an impact and report the minimum thickness of the gas film trapped under an impacting drop (§ 3). In § 4, we model the

Drop impact on superheated surfaces

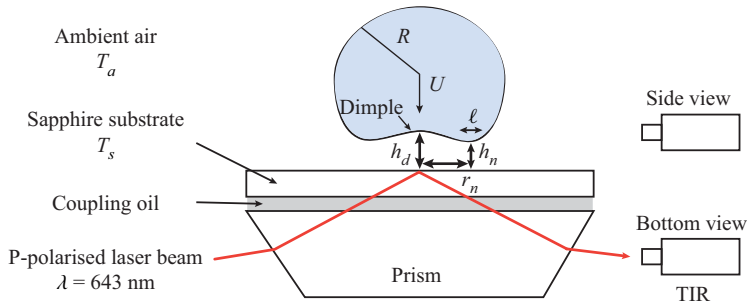


Figure 1. Ethanol drops with equilibrium radius R and velocity U impact a sapphire substrate with temperature T_s . We record side views and use total internal reflection (TIR) imaging to measure the thickness of the gas film squeezed between the liquid and the solid with two synchronised high-speed cameras. We sketch (not to scale) the typical deformation of the drop bottom interface and define the dimple height h_d , the neck height h_n , its width ℓ and its radial position r_n .

evolution of the drop interface from an initially spherical shape to a dimple shape at its closest point of approach, and derive scaling relations accounting for the thickness of the gas layer in both the capillarity and nonlinear advection dominated regimes. The paper ends with conclusions and an outlook in § 5.

2. Experimental set-up and control parameters

2.1. Set-up

In this paper, we include and complement the data presented in Chantelot & Lohse (2021), by extending them to higher surface temperatures and impact velocities. Our experiments (sketched in figure 1) consist of impacting ethanol drops on an optically smooth heated sapphire substrate (thermal conductivity, $k_s = 35 \text{ W K}^{-1} \text{ m}^{-1}$). The ethanol–sapphire combination allows us to neglect vapour cooling effects during impact, leading us to assume approximately isothermal substrate conditions (Van Limbeek *et al.* 2016, 2017). The substrate temperature T_s is set to a fixed value between 22 and 300 °C, allowing us to determine the superheat $\Delta T = T_s - T_b$, where $T_b = 78 \text{ °C}$ is the boiling temperature of ethanol. Drops with radius $R = 1.1 \pm 0.1 \text{ mm}$ are released from a calibrated needle, whose height is adjusted to obtain impact velocities U ranging from 0.3 to 1.6 m s^{-1} . Table 1 gives an overview of the properties of the liquid, with subscript l , and of the two components of the gas phase: air and ethanol vapour, with subscripts a and v , respectively. Note that the material properties of the fluids are temperature dependent (see Appendix A) and the temperature at which they should be evaluated will be discussed throughout the manuscript.

We study the impact dynamics using two synchronised high-speed cameras to obtain side views and interferometric measurements of the gas film (figure 1). We record side views at 20 000 frames per second (Photron Fastcam SA1.1) from which we determine the drop radius R and the impact velocity U . We measure the gas film thickness using total internal reflection (TIR) imaging which gives quantitative absolute thickness measurements, provided the liquid–solid distance is of the order of the evanescent length scale (Kolinski *et al.* 2012; Shirota *et al.* 2017). Practically, TIR imaging enables us to measure film thicknesses ranging from a few tens to a few hundreds of nanometres, and to accurately monitor the occurrence of liquid–solid contact. The resulting images are

	Description	Ethanol (<i>l</i>)	Ethanol (<i>v</i>)	Air
	Temperature (°C)	20	78	20
ρ	density (kg m ⁻³)	789	1.63	1.2
η	viscosity (mPa s)	1.2	1.05×10^{-2}	1.85×10^{-2}
C_p	specific heat (kJ kg ⁻¹ K ⁻¹)	2.4	1.8	1.0
k	thermal conductivity (W K ⁻¹ m ⁻¹)	0.171	0.023	0.026
κ	thermal diffusivity (m ² s ⁻¹)	0.09×10^{-6}	7.8×10^{-6}	21.7×10^{-6}
\mathcal{L}	latent heat (kJ kg ⁻¹)	853	—	—
γ	surface tension (N m ⁻¹)	0.022	—	—

Table 1. Physical properties of ethanol in the liquid (*l*) and vapour (*v*) phases and of air.

recorded at a frame rate ranging from 225 000 to 480 000 frames per second (Photron Nova S12), which we checked to be sufficient to accurately monitor the gas film dynamics, using a long distance microscope with typical resolution 10 $\mu\text{m px}^{-1}$. Details of the optical set-up, image processing and calibration of TIR measurements are given in Chantelot & Lohse (2021).

2.2. Control parameters

To identify the relevant physical effects for our choice of experimental parameters, we define and compute the values of the Weber, Reynolds, Stokes and Jakob numbers as independent variables

$$We = \frac{\rho_l R U^2}{\gamma}, \quad Re = \frac{\rho_l R U}{\eta_l}, \quad St = \frac{\rho_l R U}{\eta_g}, \quad Ja = \frac{C_{p,l}(T_b - T_a)}{\mathcal{L}}. \quad (2.1a-d)$$

Note that our definition of the Stokes number, which compares inertial effects in the liquid with viscous effects in the gas (denoted by the subscript *g*), is the inverse of that of Mandre *et al.* (2009), but consistent with other publications on the subject.

For millimetre sized ethanol drops, the chosen range of impact velocities corresponds to $We \gg 1$, $Re \gg 1$ and $St \gg 1$, indicating that inertia dominates capillary and viscous effects. The low value of the Ohnesorge number, $Oh = \sqrt{We}/Re = 0.008$, further suggests that viscosity is negligible compared with capillarity. Finally, the Jakob number, which compares the sensible heat with the latent heat, takes the value $Ja = 0.16$ so that we will assume the energetic cost of evaporation to be dominant compared with the cost of transiently heating the liquid to its boiling point (Shi *et al.* 2019).

3. Phenomenology

3.1. Sequence of events

In figure 2(a), we show side view snapshots of the impact of an ethanol drop with radius $R = 1.1$ mm and impact velocity $U = 1.2$ m s⁻¹ (i.e. $We = 57$) on a substrate heated at $T_s = 295$ °C. We focus on the first instants of the interaction between the liquid and the substrate, that is for $t \ll \tau_i$, where $\tau_i = R/U$ is the inertial time scale, a quantity of the order of a millisecond here.

While side views only expose the radial spreading of the liquid on the inertial time scale, the bottom view TIR snapshots, that display both the original grey scale images and the calculated height fields, reveal the presence of the gas film that mediates the

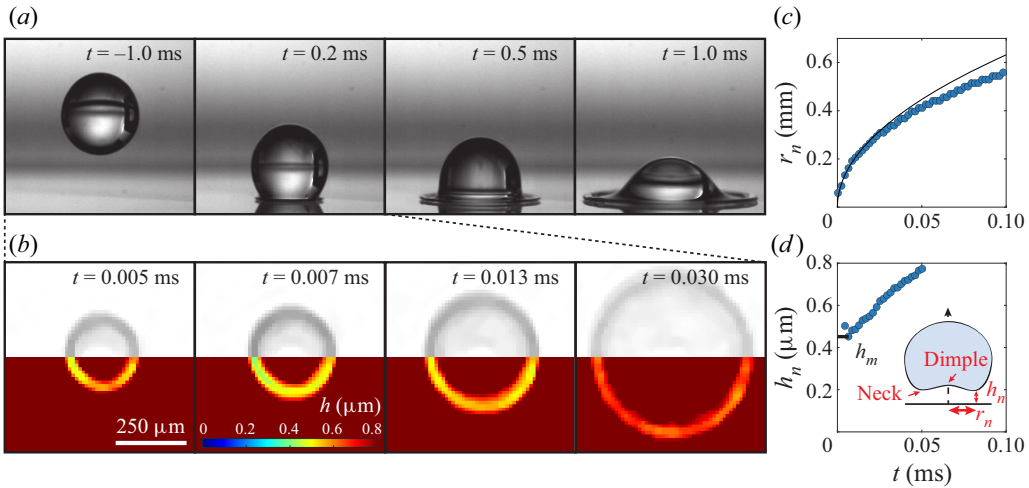


Figure 2. (a) Short-time side view snapshots of the impact of an ethanol drop with $R = 1.1 \text{ mm}$ and $U = 1.2 \text{ m s}^{-1}$ (i.e. $We = 57$) on a substrate heated at $T_s = 295 \text{ }^\circ\text{C}$. Note that the side view is recorded at a small angle from the horizontal. (b) TIR snapshots for the impact pictured in (a). We show both the original grey scale frame and the reconstructed height field with a cutoff height of $0.8 \text{ } \mu\text{m}$. The origin of time is obtained by computing the estimated instant t_0 at which the drop centre would contact the solid in the absence of air $t_0 = r_{n,0}^2/(3RU)$, where $r_{n,0}$ is the neck radius at the first instant the liquid enters within the evanescent length scale. (c) Time evolution of the azimuthally averaged neck radius $r_n(t)$ extracted from the TIR snapshots shown in (b). The solid line represents the prediction $r_n(t) = \sqrt{3URt}$ (Riboux & Gordillo 2014). (d) Azimuthally averaged neck height $h_n(t)$. We denote by h_m the azimuthally averaged minimum film thickness at short time. Movies (S1–S2) are in the supplementary movies available at <https://doi.org/10.1017/jfm.2023.290>.

drop–substrate interaction (figure 2b). The drop appears as a ring, evidencing that, as it interacts with the substrate, the liquid–gas interface deforms from its initially spherical shape to that of a dimple bordered by a region of high local curvature closest to the substrate (the neck, see the inset of figure 2(d) and Mandre *et al.* 2009; Hicks & Purvis 2010; Bouwhuis *et al.* 2012). This region, the so-called neck, moves downwards and radially outwards until the minimum thickness is reached ($t = 0.007 \text{ ms}$). Contrasting with impacts on non-superheated substrates, we observe that the neck’s vertical motion later reverses: it moves upwards as it spreads radially ($t = 0.013 \text{ ms}$ and $t = 0.030 \text{ ms}$), a marker of the influence of vapour generation.

We characterise the neck motion by tracking the azimuthally averaged neck radius $r_n(t)$ (figure 2c) and height $h_n(t) = h(r_n(t), t)$ (figure 2d). As expected, the neck radius follows the prediction $r_n(t) = \sqrt{3URt}$. The deviation from the prediction at long times is not systematic in our data, and here it can be attributed to the prolate shape of the drop at impact (see figure 2(a), $t = 0.2 \text{ ms}$). This agreement indicates the relevance of the description of impacts derived under the assumption of the absence of an intervening gas layer (Riboux & Gordillo 2014; Gordillo *et al.* 2019), and the negligible influence of vapour generation on the radial dynamics (Shirota *et al.* 2016; Chantelot & Lohse 2021). Note that the time origin is obtained by computing the estimated instant t_0 at which the drop centre would contact the solid in the absence of air $t_0 = r_{n,0}^2/(3RU)$, where $r_{n,0}$ is the neck radius at the first instant the liquid enters within the evanescent length scale. Tracking the azimuthally averaged neck height $h_n(t)$ allows us to determine the azimuthally averaged minimum gas film thickness h_m (figure 2d). We now focus on identifying the effect of the

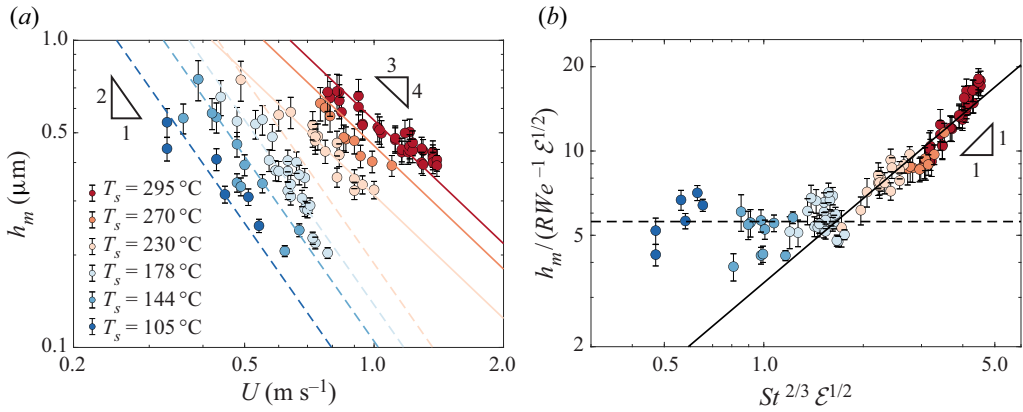


Figure 3. (a) Minimum film thickness h_m as a function of the impact velocity U for substrate temperatures T_s ranging from 105 to 295 °C. The dashed lines represent the prediction in the capillary regime (4.12) with prefactor 5.6 ± 0.8 , and the solid lines stand for the prediction in the nonlinear advection regime (4.13) with prefactor 3.4 ± 0.3 . The error bars are empirically determined from the calibration of the TIR set-up against a concave lens of known radius of curvature (see Chantelot & Lohse 2021). (b) Plot of the minimum film thickness compensated by the prediction of (4.12), $h_m / (RWe^{-1} \epsilon^{1/2})$, as a function of $St^{2/3} \epsilon^{1/2}$, highlighting the transition from the capillary dominated regime (dashed line), to the advection dominated regime (solid line).

impact velocity U and the substrate temperature T_s on h_m . Indeed, in contrast to the radial dynamics, the vertical motion of the neck is strongly affected by evaporation.

3.2. Minimum film thickness

In figure 3(a), we plot the minimum gas film thickness h_m as a function of the impact velocity for T_s varying from 105 to 295 °C. The minimum distance separating the liquid from the solid is of the order of a few hundred nanometres, and we do not observe film thicknesses below 200 nm due to the occurrence of liquid–solid contact driven by isolated surface asperities or contamination (De Ruiter *et al.* 2012; Kolinski *et al.* 2014a; Chantelot & Lohse 2021).

The minimum thickness is strongly affected by the substrate temperature: at fixed impact velocity, h_m monotonically increases with increasing superheat. For fixed T_s and R , the data suggest a power-law decay of h_m with U , $h_m \propto U^{-\alpha}$. The exponent associated with this power-law decay decreases as larger impact velocities are probed and the substrate temperature is increased. Indeed, while from $T_s = 105$ to $T_s = 178^\circ\text{C}$ the observed exponent is in agreement with the value $\alpha = 2.0 \pm 0.2$ reported by Chantelot & Lohse (2021), the data suggest that α deviates from this value at larger superheat and impact velocities. Qualitatively, this behaviour is reminiscent of that observed by Mandre & Brenner (2012) at the transition from capillary to inertial dominance at the neck, yet it is markedly different as the strong influence of T_s discriminates this case from impacts on non-superheated substrates.

4. Modelling the minimum film thickness

We now seek to understand and predict the evolution of the minimum gas film thickness h_m with the impact velocity U and substrate temperature T_s . We model the initial approach of the drop, i.e. the evolution of the drop interface from a spherical to a dimple shape until

h_m is reached at the neck. We extend the model of Mandre *et al.* (2009), Mani *et al.* (2010) and Mandre & Brenner (2012), derived in the absence of evaporation, further building on our previous work on heated surfaces (Chantelot & Lohse 2021) by going beyond the capillary regime.

4.1. Governing equations

For completeness, we recall the equations of motion for the drop liquid and the gas film in the presence of superheat. We consider a two-dimensional geometry, following Mani *et al.* (2010), and model the drop liquid as an incompressible fluid:

$$\frac{\partial \mathbf{u}}{\partial t} + \frac{1}{\rho_l} \nabla p_l = -\mathbf{u} \cdot \nabla \mathbf{u} + \frac{\eta_l}{\rho_l} \nabla^2 \mathbf{u}, \quad \nabla \cdot \mathbf{u} = 0, \quad (4.1a,b)$$

where p_l is the liquid pressure, and $\mathbf{u} = (u_l, v_l)$ are the velocity components in the x (replacing r in this two-dimensional model) and z directions, respectively. The viscous and nonlinear inertia terms, on the right-hand side of (4.1a), are initially considered to be negligible, owing to the large liquid Reynolds number and the absence of velocity gradients in the drop during free fall, respectively. We obtain an equation for the motion of the interface $h(x, t)$ by projecting (4.1a) in the vertical direction and evaluating it at $z = 0$ (Mani *et al.* 2010):

$$\frac{\partial^2 h}{\partial t^2} + \frac{1}{\rho_l} \frac{\partial p_l}{\partial z} = - \left(u_l \frac{\partial v_l}{\partial x} + v_l \frac{\partial v_l}{\partial z} \right) + \frac{\eta_l}{\rho_l} \left(\frac{\partial^2 v_l}{\partial x^2} + \frac{\partial^2 v_l}{\partial z^2} \right) - \frac{\partial}{\partial t} \left(u_l \frac{\partial h}{\partial x} \right), \quad (4.2)$$

where we used the kinematic boundary condition $\partial h / \partial t = v_l - u_l \partial h / \partial x$.

Next, we describe the flow in the gas layer. We do not take into account gas compressibility and non-continuum effects which set in at larger impact speeds than those probed in this study (Mandre & Brenner 2012). We use the viscous lubrication approximation as the gas film is thin, $h \ll R$, and the typical value of the gas Reynolds number $Re_g = \rho_g h U / \eta_g$ is much smaller than one. It reads

$$\frac{\partial h}{\partial t} - \frac{1}{12\eta_g} \frac{\partial}{\partial x} \left(h^3 \frac{\partial p_g}{\partial x} \right) = \frac{1}{\rho_g} \frac{k_g \Delta T}{\mathcal{L}h} - \frac{1}{2} \frac{\partial}{\partial x} (u_l h), \quad (4.3)$$

where p_g is the gas pressure and we have again used the kinematic boundary condition. The influence of evaporation appears as a source term, derived under the assumptions of (i) conductive heat transfer through the gas layer, and (ii) dominant energetic cost of latent heat compared with sensible heat (i.e. $Ja \ll 1$) (Biance, Clanet & Quéré 2003; Sobac *et al.* 2014; Chantelot & Lohse 2021).

Finally, the liquid and gas pressures are related by the Laplace pressure jump at the interface:

$$p_l - p_g = \gamma \kappa, \quad (4.4)$$

where $\kappa = \partial^2 h / \partial x^2 / (1 + (\partial h / \partial x)^2)^{3/2}$ is the interface curvature.

4.2. Dominant balance

To identify the relevant contributions, it is convenient to non-dimensionalise equations (4.2)–(4.4) using the scales involved in dimple formation (Mandre *et al.* 2009; Hicks & Purvis 2010; Mani *et al.* 2010; Bouwhuis *et al.* 2012), that have also been shown to

be relevant for impacts on superheated substrates (Chantelot & Lohse 2021). Using the transformations

$$\left. \begin{aligned} (x, z) &= RSt^{-1/3}(\tilde{x}, \tilde{z}), \quad h = RSt^{-2/3}\tilde{h}, \quad \mathbf{u} = U\tilde{\mathbf{u}}, \\ t &= \frac{RSt^{-2/3}}{U}\tilde{t}, \quad (p_l, p_g) = \frac{\eta_g U}{RSt^{-4/3}}(\tilde{p}_l, \tilde{p}_g), \end{aligned} \right\} \quad (4.5a-e)$$

the governing equations become

$$\frac{\partial^2 \tilde{h}}{\partial \tilde{t}^2} + \frac{\partial \tilde{p}_l}{\partial \tilde{z}} = \frac{1}{Re} \left(\frac{\partial^2 \tilde{v}_l}{\partial \tilde{x}^2} + \frac{\partial^2 \tilde{v}_l}{\partial \tilde{z}^2} \right) - St^{-1/3} \left(\tilde{u}_l \frac{\partial \tilde{v}_l}{\partial \tilde{x}} + \tilde{v}_l \frac{\partial \tilde{v}_l}{\partial \tilde{z}} + \frac{\partial}{\partial \tilde{t}} \left(\tilde{u}_l \frac{\partial \tilde{h}}{\partial \tilde{x}} \right) \right), \quad (4.6)$$

$$\frac{\partial \tilde{h}}{\partial \tilde{t}} - \frac{1}{12} \frac{\partial}{\partial \tilde{x}} \left(\tilde{h}^3 \frac{\partial \tilde{p}_g}{\partial \tilde{x}} \right) = \mathcal{E} St^{5/3} We^{-1} \tilde{h}^{-1} - \frac{1}{2} St^{-1/3} \frac{\partial}{\partial \tilde{x}} (\tilde{u}_l \tilde{h}), \quad (4.7)$$

$$\tilde{p}_l - \tilde{p}_g \approx We^{-1} St^{-1/3} \tilde{\kappa}, \quad (4.8)$$

where we introduced the evaporation number \mathcal{E} (Sobac *et al.* 2014),

$$\mathcal{E} = \frac{\eta_g k_g \Delta T}{\gamma \rho_g R \mathcal{L}}, \quad (4.9)$$

that can be understood as the ratio of the lubrication pressure originating from the evaporation source term $\eta_g k_g \Delta T / (\rho_g R^2 \mathcal{L})$ and the capillary pressure γ / R .

If the substrate is not superheated (i.e. $\mathcal{E} = 0$), (4.6)–(4.8) are identical to those obtained by Mandre & Brenner (2012), and the dominant balance is obtained from the left-hand side terms (see Appendix B). When $\mathcal{E} > 0$, the left-hand sides of (4.6) and (4.8) still contain the dominant balance as $We \gg 1$, $Re \gg 1$ and $St \gg 1$. Yet, the evaporative source term cannot be neglected *a priori* in the lubrication equation (4.7). We hypothesise that in superheated conditions the gas flow is driven by the contribution of evaporation in the neck region as the substrate temperature strongly influences the minimum thickness h_m (figure 3a), and as we estimate that the liquid–gas interface can be heated up to the liquid’s boiling point on the time scale at which h_m is reached (i.e. of the order of 10 μ s, see Appendix C). Under this assumption, the dominant balance is obtained by equating the gas pressure term and the evaporative source term in (4.7).

4.3. Neck solution

We now look for a solution of the governing equations that describes the neck motion, that is the horizontal and vertical motions of the curved region of radial extent ℓ located at $x = x_n(t)$ (x_n replacing r_n in this two-dimensional model). Using pressure continuity at the liquid–gas interface ($\tilde{p} = \tilde{p}_l = \tilde{p}_g$), as the right-hand side of (4.8) is initially negligible, we construct a solution by adopting the following self-similar ansatz in the vicinity of the neck for the interface height and the pressure:

$$\tilde{h}(\tilde{x}, \tilde{t}) = \tilde{h}_n(\tilde{t})H(\Theta), \quad \tilde{p}(\tilde{x}, \tilde{t}) = \tilde{p}_n(\tilde{t})\Pi(\Theta), \quad (4.10a,b)$$

where $\Theta(\tilde{x}, \tilde{t}) = (\tilde{x} - \tilde{x}_n(\tilde{t})) / \tilde{\ell}(\tilde{t})$ is the self-similar variable. Introducing the self-similar fields in (4.6) and (4.7), we obtain scaling relationships for the length scale and pressure at the neck from the dominant balance in superheated conditions (i.e. when $\mathcal{E} > 0$):

$$\tilde{\ell} \sim \dot{\tilde{x}}_n We St^{-5/3} \mathcal{E}^{-1} \tilde{h}_n^2, \quad \tilde{p}_n \sim \dot{\tilde{x}}_n We^{-1} St^{5/3} \mathcal{E} \tilde{h}_n^{-1}. \quad (4.11a,b)$$

To derive (4.11a,b), we assumed: (i) that the time derivatives are dominated by their advective contribution $\partial / \partial \tilde{t} \approx \dot{\tilde{x}}_n \partial / \partial \tilde{x}$, where $\dot{\tilde{x}}_n$ is a constant for a fixed set of control

parameters (Mani *et al.* 2010), and (ii) that the vertical pressure gradient in the liquid scales as $\tilde{p}_l/\tilde{\ell}$. Indeed, as the nonlinear terms on the right-hand side of (4.6) are initially negligible, \tilde{p}_l follows a Laplace equation.

Equations (4.11*a,b*) differ in two important ways from those obtained by Mani *et al.* (2010) in the absence of evaporation (B1*a,b*). (i) They explicitly involve the superheat through the influence of the evaporation number \mathcal{E} . (ii) The dependency of $\tilde{\ell}$ and \tilde{p}_n on \tilde{h}_n is modified, with the neck length scale following a power law with \tilde{h}_n with an exponent 2 instead of 3/2, and with the neck pressure following a power law with \tilde{h}_n with an exponent -1 instead of $-1/2$. Yet, with or without superheat, the horizontal extent of the neck region $\tilde{\ell}$ vanishes and the pressure \tilde{p}_n diverges as the neck thickness \tilde{h}_n decreases. Close to this divergence, it is essential to check if the self-similar solution is consistent, by assessing the importance of initially neglected physical effects. Following Mandre & Brenner (2012), we discuss the influence of capillary and nonlinear inertia effects as \tilde{h}_n tends towards zero.

4.3.1. Surface tension dominated regime

The curvature of the liquid–gas interface in the neck region, $\tilde{\kappa} \sim \tilde{h}_n/\tilde{\ell}^2$, diverges as the drop approaches the substrate. The Laplace pressure associated with this curvature, proportional to \tilde{h}_n^{-3} , diverges faster than the neck pressure, which evolves as \tilde{h}_n^{-1} . Capillary effects regularise the interfacial singularity as the Laplace pressure becomes of the order of the neck pressure, setting the minimum thickness of the gas film:

$$\frac{h_m}{R} \sim We^{-1} \mathcal{E}^{1/2}, \quad (4.12)$$

as already derived in Chantelot & Lohse (2021). For a fixed drop radius and superheat, (4.12) predicts a power-law decrease of the minimum thickness with the impact velocity, $h_m \propto U^{-2}$, that differs from that obtained for non-superheated impacts, $h_m \propto U^{-20/9}$ (B2). This power law is in qualitative agreement with the experimental data for $T_s \leq 178^\circ\text{C}$. Equation (4.12) also predicts the increase of the minimum thickness with the superheat, $h_m \propto \Delta T^{1/2}$ for fixed impact parameters and material properties. Yet, the dependence of h_m on ΔT is not directly given by a power law, as the material properties are temperature dependent. To quantitatively test the influence of ΔT , we take into account the temperature dependence of the gas properties and the reduced surface tension of the liquid–gas interface heated at its boiling point ($\gamma = 0.017 \text{ N m}^{-1}$ at T_b). We evaluate the gas viscosity η_g , thermal conductivity k_g and density ρ_g at $(T_s + T_b)/2$, as the conduction time scale $h^2 \rho_g C_{p,g}/k_g \approx 0.1 \mu\text{s}$ suggests that steady state conductive heat transfer is applicable in the gas layer, and we further assume that, in the neck region, the gas phase is constituted of ethanol vapour. In figure 3(*a*), we plot the prediction of (4.12) with a prefactor 5.6 ± 0.8 obtained from a fit of the data for $T_s \leq 178^\circ\text{C}$ (dashed lines). The scaling relation quantitatively captures the temperature dependence of the minimum thickness h_m , as well as its decrease with increasing impact velocity for $T_s \leq 178^\circ\text{C}$. However, the data for larger superheat deviate from the expected scaling relationship, as evidenced by plotting (4.12) for $T_s = 230^\circ\text{C}$ (dashed line). We now rationalise this deviation.

4.3.2. Nonlinear advection dominated regime

Similarly as for the interface curvature, the nonlinear advective term diverges as the thickness at the neck vanishes. Equation (4.6) allows us to estimate the pressure associated

with the nonlinear advective term which scales as $St^{-1/3}\tilde{h}_n^2/\tilde{\ell}^2$, assuming that $\tilde{v}_l \sim \partial\tilde{h}_n/\partial\tilde{t}$ and that the time derivatives are advection dominated (Mandre & Brenner 2012). Using (4.11a), which relates the neck length scale $\tilde{\ell}$ to the neck height \tilde{h}_n , we find that this pressure is proportional to \tilde{h}_n^{-2} , indicating that it blows up faster than the neck pressure $\tilde{p}_n \propto \tilde{h}_n^{-1}$. Nonlinear effects come into play as the pressure associated with nonlinear advection becomes of the same order as the neck pressure \tilde{p}_n (4.11b), giving a scaling relation for the minimum thickness:

$$\frac{h_m}{R} \sim We^{-1}St^{2/3}\mathcal{E}. \quad (4.13)$$

Equation (4.13) predicts a power-law decrease of the minimum thickness with the impact velocity, $h_m \propto U^{-4/3}$, for a fixed drop radius and superheat. The exponent associated with this power-law decay is lower than that identified in the capillary regime, where $h_m \propto U^{-2}$, in qualitative agreement with our measurements, and it is equal to that reported by Mandre & Brenner (2012) in the advection dominated regime (B3). For fixed impact parameters and material properties, (4.13) also predicts the increase of h_m with ΔT , $h_m \propto \Delta T$, which is stronger than in the surface tension dominated regime (where $h_m \propto \Delta T^{1/2}$). Taking into account the temperature dependence of the material properties, we plot in figure 3(a) the predictions of (4.13) for $T_s > 178^\circ\text{C}$ (solid lines). The data are in quantitative agreement with the proposed scaling relation, with a prefactor 3.4 ± 0.3 which we determine from fitting the data for $T_s > 178^\circ\text{C}$.

The transition from the dominance of capillary to nonlinear inertia effects is expected when the predictions of (4.12) and (4.13) are equal, i.e. when $St^{2/3}\mathcal{E}^{1/2}$ is of order one. We evidence this transition by reporting in figure 3(b) the minimum thickness h_m normalised by the capillary scaling (4.12) as a function of $St^{2/3}\mathcal{E}^{1/2}$. This compensated plot highlights the systematic deviation from the scaling relation obtained in the capillary regime (dashed black line, (4.12)) when $St^{2/3}\mathcal{E}^{1/2} \gtrsim 1$, and reiterates that this deviation is quantitatively captured by the introduction of the nonlinear inertia dominated regime (solid black line, (4.13)).

5. Conclusion and outlook

In this contribution, we experimentally evidence that nonlinear advection, similarly to capillarity, contributes to prevent liquid–solid contact during drop impact. We reveal the existence of the nonlinear inertia dominated regime, theoretically predicted by Mandre & Brenner (2012), but obscured in experiments by the occurrence of liquid–solid contact, by measuring the minimum thickness of the gas film trapped under drops impacting on superheated surfaces. We show that, for large impact velocities and substrate temperatures, the minimum thickness systematically deviates from the scaling relation predicted when assuming that capillarity dominates the behaviour in the neck region, closest to the substrate. We quantitatively capture this deviation by taking into account the influence of nonlinear advection, allowing us to derive a scaling relation for the minimum thickness in the high temperature and velocity regime. Performing impacts in the dynamical Leidenfrost regime allows us to uncover the nonlinear advection dominated regime not only by enabling us to probe contactless drop–substrate interactions for a large range of impact velocities and substrate temperatures, but also by altering the nature of the flow in the gas layer. Indeed, the presence of evaporation leads to a modified dominant balance at the neck, effectively putting the transition from the capillary to the advective regime within the experimentally accessible regime.

Future work should focus on building our physical understanding of the hydrodynamics obviating the need for gas film drainage, that is on describing the influence of capillarity and nonlinear advection beyond their ability to regularise the neck singularity. In doing so, it will be of particular interest to investigate the influence of liquid viscosity on the early dynamics of the drop impact process which displays a hitherto unexplained lift-off behaviour (Kolinski, Mahadevan & Rubinstein 2014*b*; Mishra, Rubinstein & Rycroft 2022).

Supplementary movies. Supplementary movies are available at <https://doi.org/10.1017/jfm.2023.290>.

Acknowledgements. We thank C. Datt and J.M. Gordillo for fruitful discussions.

Funding. We acknowledge funding from the ERC Advanced Grant DDD under grant no. 740479.

Declaration of interests. The authors report no conflict of interest.

Author ORCIDs.

 Pierre Chantelot <https://orcid.org/0000-0003-1342-2539>;

 Detlef Lohse <https://orcid.org/0000-0003-4138-2255>.

Appendix A. Variation of the physical properties with temperature

In this section, we report on the determination of the temperature dependence of the physical properties used throughout the manuscript. On the one hand, we take the temperature dependent surface tension γ , liquid viscosity η_l and vapour thermal conductivity k_v from tabulated values out of the Dortmund Data Bank. On the other hand, we estimate the vapour density ρ_v by treating the vapour as an ideal gas:

$$\rho_v(T) = \frac{P_0 M}{R_g T}, \quad (\text{A1})$$

where P_0 is the atmospheric pressure, M the molar mass and R_g the universal gas constant.

The temperature dependence of the vapour viscosity is given by the kinetic gas theory as

$$\frac{\eta_v(T)}{\eta_v(T_b)} = \sqrt{\frac{T}{T_b}}, \quad (\text{A2})$$

where the value $\eta_v(T_b) = 10.5 \mu\text{Pa s}$ is taken from Silgado & Storrow (1950).

Appendix B. Minimum thickness for impacts in the absence of evaporation

In the absence of evaporation (i.e. for $\mathcal{E} = 0$), the dominant balance is given by the terms on the left-hand sides of (4.6), (4.7) and (4.8) as $We \gg 1$, $Re \gg 1$ and $St \gg 1$. Looking for a similarity solution at the neck gives the following scaling relations linking the pressure \tilde{p}_n and the length scale $\tilde{\ell}$ to the thickness \tilde{h}_n (Mandre *et al.* 2009; Mani *et al.* 2010; Mandre & Brenner 2012):

$$\tilde{\ell} \sim \dot{x}_n^{1/2} \tilde{h}_n^{3/2}, \quad \tilde{p}_n \sim \dot{x}_n^3 \tilde{h}_n^{-1/2}. \quad (\text{B1a,b})$$

As \tilde{h}_n decreases, the initially neglected capillary and nonlinear effects can regularise the singularity. Indeed, the Laplace pressure at the neck diverges as \tilde{h}_n^{-2} (4.8), faster than \tilde{p}_n , indicating that the initial hypothesis neglecting surface tension is no longer valid as

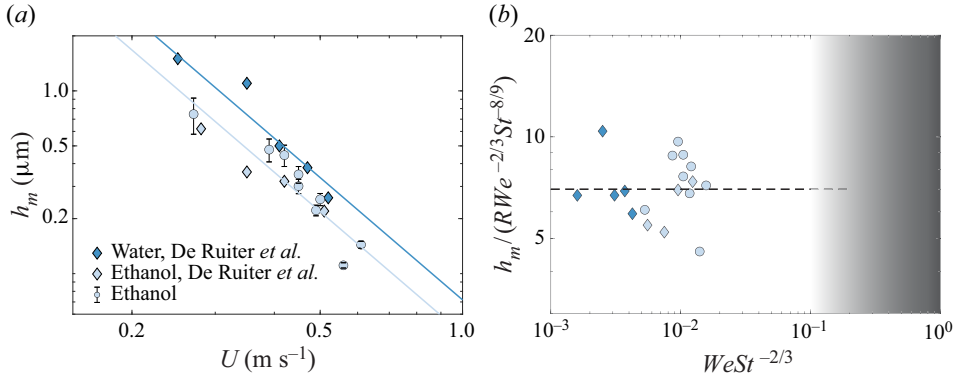


Figure 4. (a) Minimum film thickness h_m in the absence of superheat for water and ethanol drop impacts on glass substrates extracted from the work of De Ruiter *et al.* (2012) (dark and light blue diamonds, respectively) and for ethanol drop impacts on freshly cleaved mica substrates (light blue circles). The solid lines represent the predictions of (B2) with prefactor 7. (b) Minimum film thickness on room temperature substrates compensated by the prediction of (B2) as a function of $WeSt^{-2/3}$. The data collapse onto a constant in the surface tension dominated regime, and we do not probe large enough impact velocities to reach the advection dominated region (grey shaded area).

the drop approaches the solid, and setting the minimum thickness in the surface tension dominated regime:

$$\frac{h_m}{R} \sim We^{-2/3} St^{-8/9}. \tag{B2}$$

Similarly, the advective contribution $\tilde{\mathbf{u}} \cdot \nabla \tilde{\mathbf{u}}$ diverges as $\tilde{h}_n^{-5/2}$, faster than the liquid pressure gradient. The breakdown of the similarity solution in the nonlinear inertia dominated regime occurs for

$$\frac{h_m}{R} \sim St^{-4/3}, \tag{B3}$$

and we expect to observe the transition from the surface tension dominated regime to the advection dominated regime for $WeSt^{-2/3} \approx 1$.

In figure 4(a), we plot the minimum thickness for the impact of water and ethanol drops on room temperature glass substrates measured by De Ruiter *et al.* (2012) and for the impact of ethanol drops on room temperature mica substrates performed in the context of this study. The data for both water and ethanol drops are compatible with the predictions of (B2). Indeed, all experiments fulfil the condition $WeSt^{-2/3} \ll 1$, suggesting that they lie in the capillary regime (figure 4b). The occurrence of liquid–solid contact prevents us from observing the nonlinear inertia dominated regime for these impacts in the absence of evaporation.

Appendix C. Initial heating of the liquid–gas interface

We estimate the time needed for the drop’s liquid–gas interface to reach the boiling temperature using a one-dimensional heat transfer model that we sketch in figure 5. As discussed in the main text, steady state conductive heat transfer is applicable in the gas layer, enabling us to compute the heat flux transferred from the wall to the liquid as $q_w = k_g(T_s - T_i)/h$, where T_i is the temperature of the interface. On the contrary, in the liquid, a thermal boundary layer with thickness $l_T \sim \sqrt{\kappa_l t}$ forms, allowing us to estimate the heat flux received by the liquid as $q_l \sim k_l(T_i - T_a)/l_T$. When the interface temperature

Drop impact on superheated surfaces

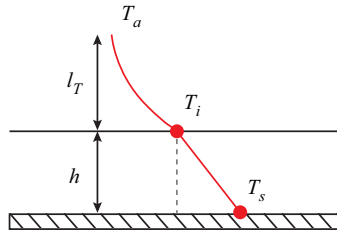


Figure 5. Sketch of the one-dimensional heat transfer model used to estimate the time needed for the interface temperature T_i to reach the liquid boiling temperature T_b .

is below T_b , the wall heat flux is used only to heat liquid; $q_w \sim q_l$, giving an expression for the time τ needed for the liquid–gas interface to reach T_b :

$$\tau \sim \frac{1}{\kappa_l} \left(\frac{k_l}{k_g} \right)^2 \left(\frac{T_b - T_a}{T_s - T_b} \right)^2 h^2. \quad (\text{C1})$$

We estimate τ taking the liquid thermal diffusivity $\kappa_l = 0.09 \times 10^6 \text{ m}^2 \text{ s}^{-1}$ and thermal conductivity $k_l = 0.171 \text{ W m}^{-1} \text{ K}^{-1}$ at room temperature, and the air properties at $(T_s + T_b)/2$ (for $T_i < T_b$, we assume little vapour is produced). For $T_s = 200^\circ \text{C}$ and $h = 0.5 \mu\text{m}$, we find $\tau \approx 15 \mu\text{s}$, a value compatible with the time at which h_m is reached, where we observe a strong influence of vapour generation.

Finally, we stress that this one-dimensional model oversimplifies the heat transfer problem by neglecting both the geometry of the vapour layer, and its temporal variation. We believe that the strong influence of temperature, and thus of evaporation, on the minimum neck thickness h_m is the key observation that justifies assuming that the interface can be heated to T_b within a time of the order of $10 \mu\text{s}$.

REFERENCES

- BIANCE, A.-L., CLANET, C. & QUÉRÉ, D. 2003 Leidenfrost drops. *Phys. Fluids* **15** (6), 1632–1637.
- BOUWHUIS, W., VAN DER VEEN, R.C.A., TRAN, T., KEIJ, D.L., WINKELS, K.G., PETERS, I.R., VAN DER MEER, D., SUN, C., SNOEIJER, J.H. & LOHSE, D. 2012 Maximal air bubble entrainment at liquid-drop impact. *Phys. Rev. Lett.* **109** (26), 264501.
- BREITENBACH, J., ROISMAN, I.V. & TROPEA, C. 2018 From drop impact physics to spray cooling models: a critical review. *Exp. Fluids* **59** (3), 55.
- CHANDRA, S. & AVEDISSIAN, C.T. 1991 On the collision of a droplet with a solid surface. *Proc. R. Soc. Lond. A* **432** (1884), 13–41.
- CHANTELOT, P. & LOHSE, D. 2021 Drop impact on superheated surfaces: short-time dynamics and transition to contact. *J. Fluid Mech.* **928**, A36.
- CHUBYNSKY, M.V., BELOUSOV, K.I., LOCKERBY, D.A. & SPRITTLES, J.E. 2020 Bouncing off the walls: the influence of gas-kinetic and van der Waals effects in drop impact. *Phys. Rev. Lett.* **124**, 084501.
- DE RUITER, J., OH, J.M., VAN DEN ENDE, D. & MUGELE, F. 2012 Dynamics of collapse of air films in drop impact. *Phys. Rev. Lett.* **108** (7), 074505.
- DRISCOLL, M.M. & NAGEL, S.R. 2011 Ultrafast interference imaging of air in splashing dynamics. *Phys. Rev. Lett.* **107** (15), 154502.
- DUCHEMIN, L. & JOSSERAND, C. 2011 Curvature singularity and film-skating during drop impact. *Phys. Fluids* **23** (9), 091701.
- GORDILLO, J.M., RIBOUX, G. & QUINTERO, E.S. 2019 A theory on the spreading of impacting droplets. *J. Fluid Mech.* **866**, 298–315.
- HARVEY, D., HARPER, J.M. & BURTON, J.C. 2021 Minimum Leidenfrost temperature on smooth surfaces. *Phys. Rev. Lett.* **127** (10), 104501.
- HICKS, P.D. & PURVIS, R. 2010 Air cushioning and bubble entrapment in three-dimensional droplet impacts. *J. Fluid Mech.* **649**, 135–163.

- JOSSERAND, C. & THORODDSEN, S.T. 2016 Drop impact on a solid surface. *Annu. Rev. Fluid Mech.* **48**, 365–391.
- KIM, J. 2007 Spray cooling heat transfer: the state of the art. *Intl J. Heat Fluid Flow* **28** (4), 753–767.
- KOLINSKI, J.M., MAHADEVAN, L. & RUBINSTEIN, S.M. 2014a Drops can bounce from perfectly hydrophilic surfaces. *Europhys. Lett.* **108** (2), 24001.
- KOLINSKI, J.M., MAHADEVAN, L. & RUBINSTEIN, S.M. 2014b Lift-off instability during the impact of a drop on a solid surface. *Phys. Rev. Lett.* **112** (13), 134501.
- KOLINSKI, J.M., RUBINSTEIN, S.M., MANDRE, S., BRENNER, M.P., WEITZ, D.A. & MAHADEVAN, L. 2012 Skating on a film of air: drops impacting on a surface. *Phys. Rev. Lett.* **108** (7), 074503.
- LAAN, N., DE BRUIN, K.G., BARTOLO, D., JOSSERAND, C. & BONN, D. 2014 Maximum diameter of impacting liquid droplets. *Phys. Rev. Appl.* **2** (4), 044018.
- LEIDENFROST, J.G. 1756 *De aquae communis nonnullis qualitatibus tractatus*. Ovenius.
- LOHSE, D. 2022 Fundamental fluid dynamics challenges in inkjet printing. *Annu. Rev. Fluid Mech.* **54**, 349–382.
- MANDRE, S. & BRENNER, M.P. 2012 The mechanism of a splash on a dry solid surface. *J. Fluid Mech.* **690**, 148.
- MANDRE, S., MANI, M. & BRENNER, M.P. 2009 Precursors to splashing of liquid droplets on a solid surface. *Phys. Rev. Lett.* **102** (13), 134502.
- MANI, M., MANDRE, S. & BRENNER, M.P. 2010 Events before droplet splashing on a solid surface. *J. Fluid Mech.* **647** (1), 163–185.
- MISHRA, S., RUBINSTEIN, S.M. & RYCROFT, C.H. 2022 Computing the viscous effect in early-time drop impact dynamics. *J. Fluid Mech.* **945**, A13.
- PAN, K.L. & LAW, C.K. 2007 Dynamics of droplet–film collision. *J. Fluid Mech.* **587**, 1–22.
- QUÉRÉ, D. 2013 Leidenfrost dynamics. *Annu. Rev. Fluid Mech.* **45**, 197–215.
- REYNOLDS, O. 1881 On the floating of drops on the surface of water depending only on the purity of the surface. *Proc. Manch. Lit. Philos. Soc.* **21** (1), 413–414.
- RIBOUX, G. & GORDILLO, J.M. 2014 Experiments of drops impacting a smooth solid surface: a model of the critical impact speed for drop splashing. *Phys. Rev. Lett.* **113** (2), 024507.
- SHI, M., FRANK, F., WANG, L., XU, F., LU, T.J. & GRIGOROPOULOS, C.P. 2019 Role of Jakob number in Leidenfrost phenomena unveiled by theoretical modeling. *Phys. Fluids* **31** (4), 042109.
- SHIROTA, M., VAN LIMBEEK, M.A.J., LOHSE, D. & SUN, C. 2017 Measuring thin films using quantitative frustrated total internal reflection (FTIR). *Eur. Phys. J. E* **40** (5), 54.
- SHIROTA, M., VAN LIMBEEK, M.A.J., SUN, C., PROSPERETTI, A. & LOHSE, D. 2016 Dynamic Leidenfrost effect: relevant time and length scales. *Phys. Rev. Lett.* **116** (6), 064501.
- SILGARDO, R.B. & STORROW, J.A. 1950 Viscosity of mixed vapours. *J. Soc. Chem. Ind.* **69** (9), 261–266.
- SOBAC, B., REDNIKOV, A., DORBOLO, S. & COLINET, P. 2014 Leidenfrost effect: accurate drop shape modeling and refined scaling laws. *Phys. Rev. E* **90** (5), 053011.
- SWITKES, M., ROTHSCHILD, M., SHEDD, T.A., BURNETT, H.B. & YEUNG, M.S. 2005 Bubbles in immersion lithography. *J. Vac. Sci. Technol. B* **23** (6), 2409–2412.
- THORODDSEN, S.T., ETOH, T.G., TAKEHARA, K., OOTSUKA, N. & HATSUKI, Y. 2005 The air bubble entrapped under a drop impacting on a solid surface. *J. Fluid Mech.* **545**, 203–212.
- TRAN, T., STAAT, H.J.J., PROSPERETTI, A., SUN, C. & LOHSE, D. 2012 Drop impact on superheated surfaces. *Phys. Rev. Lett.* **108** (3), 036101.
- VAN LIMBEEK, M.A.J., SCHAARSBERG, M.H.K., SOBAC, B., REDNIKOV, A., SUN, C., COLINET, P. & LOHSE, D. 2017 Leidenfrost drops cooling surfaces: theory and interferometric measurement. *J. Fluid Mech.* **827**, 614–639.
- VAN LIMBEEK, M.A.J., SHIROTA, M., SLEUTEL, P., SUN, C., PROSPERETTI, A. & LOHSE, D. 2016 Vapour cooling of poorly conducting hot substrates increases the dynamic Leidenfrost temperature. *Intl J. Heat Mass Transfer* **97**, 101–109.
- VAN DER VEEN, R.C., TRAN, T., LOHSE, D. & SUN, C. 2012 Direct measurements of air layer profiles under impacting droplets using high-speed color interferometry. *Phys. Rev. E* **85** (2), 026315.
- WILDEMAN, S., VISSER, C.W., SUN, C. & LOHSE, D. 2016 On the spreading of impacting drops. *J. Fluid Mech.* **805**, 636–655.
- XU, L., ZHANG, W.W. & NAGEL, S.R. 2005 Drop splashing on a dry smooth surface. *Phys. Rev. Lett.* **94** (18), 184505.
- YARIN, A.L. 2006 Drop impact dynamics: splashing, spreading, receding, bouncing. *Annu. Rev. Fluid Mech.* **38**, 159–192.